Nanoscale

PAPER

View Article Online
View Journal | View Issue

Cite this: *Nanoscale*, 2014, **6**, 12655

Fine structural tuning of whereabout and clustering of metal–metal oxide heterostructure for optimal photocatalytic enhancement and stability†

Minmin Gao,[a] Connor Kang Nuo Peh,[a] Yanlin Pan,[b] Qing-Hua Xu[b] and Ghim Wei Ho*[a,c]

Received 18th June 2014,
Accepted 6th August 2014

DOI: 10.1039/c4nr03373f

www.rsc.org/nanoscale

In this work, we demonstrate the fine structural tuning of metal–metal oxide heterostructure with regards to the individual tuning of the various core and shell components from shell thickness to metal core constitution. Furthermore, we deliberately engineered spatially confined and clustered Au nanoparticles in the core of a porous shell structure without the assistance of template or linker. Our findings unambiguously highlight that whilst it is important to incorporate metal nanoparticles into metal oxide for higher photocatalytic performance through enhanced light absorption and charge separation, the "whereabout" and clustering of Au nanoparticles affect the photocatalytic performance. Furthermore, we also prove the enhanced and prolonged catalytic activity of spatially confined metal cores over conventional surface loaded metal particles, which originates from the structural stability and optimized contact interface for heterojunction-induced charge transfer. The present well-controlled synthetic route can offer a facile and valuable way to tune and probe specific structure in relation to nanoscale light-matter manipulation and solar-to-chemical energy conversion studies.

Introduction

The development of photocatalysts with porous morphologies mainly aims to increase the specific surface area and decrease the migration distance of charge carrier, while innovation in the hetero-interfacing of photocatalyst with metal nanoparticles aims to enhance light absorption, charge separation and transfer efficiencies. The combination of these strategies can provide a powerful approach to rationally design novel material that boost light energy conversion systems such as solar cell, photoelectrochemical, photocatalysis for water splitting and environmental remediation.

In the context of hetero-interfacing, various metals with metal oxide systems have been developed.[1–5] In several cases, the metal particles are simply loaded onto the surfaces of the semiconductors as isolated island to produce limited hetero-interfaces, while more uncommonly reported is a spatial confinement of metal nanoparticle within metal oxide matrix. The confinement of the nanoparticles as core with the metal oxide shell protects and isolates the nanoparticles from leaching and coalescence during catalytic reactions. In addition, the core–shell architecture provides strong interaction between the metal core and shell that may boost catalytic activity. Furthermore, the utilization of the spatial confinement of metal nanoparticle for photochemical studies is limited. Hence, some fundamental questions that need to be address *i.e.* "whereabouts" coupling of metal nanoparticles and how the "clustering" of metal nanoparticles may affect photocatalytic properties.

There are various chemical synthesis methods of fabricating spatially confined metal particles in metal oxide system *i.e.* yolk–shell, eccentric and concentric core–shell, which include layer-by-layer deposition and sacrificial templating techniques.[6,7] Nevertheless, it is highly challenging to design and synthesize such heterostructure because of formidable difficulties in controlling its growth kinetics to achieve specific structure. It is noted that a well-controlled synthetic route can facilitate the probing of specific structure to elucidate the influence of various structural components on photochemical properties. It is also noteworthy that most of the reported synthetic processes involve the use of additional materials as a support to form the shell or a linker between the core and shell.[8–11] This is often followed by etching process to remove the supporting material and/or introduce porosity to the shell. Such multistep procedures reduce controllability in terms of metal nanoparticle core sizes and dispersivity, as well as shell porosity and crystallinity. Moreover, using additional materials

[a]*Department of Electrical and Computer Engineering, National University of Singapore, 4 Engineering Drive 3, Singapore 117576, Singapore. E-mail: elehgw@nus.edu.sg*
[b]*Department of Chemistry, National University of Singapore, 3 Science Drive 3, Singapore 117543, Singapore*
[c]*Institute of Materials Research and Engineering, A*STAR (Agency for Science, Technology and Research), 3 Research Link, Singapore 117602, Singapore*
† Electronic supplementary information (ESI) available. See DOI: 10.1039/c4nr03373f

to encapsulate metal nanoparticles may decrease the accessibility of the reactants to the active sites. Furthermore, calcination is generally carried out to convert TiO_2 from amorphous to crystalline phase or for the precipitation of metal nanoparticles, which will cause the detrimental effect of metal nanoparticles sintering leading to a loss in reactivity. Therefore, the design of highly controllable template or capping ligand free synthesis method to fabricate the core–shell heterostructure of appropriate porosity and structural stability is desirable.

Herein, we have rationally designed a metal–metal oxide heterostructure catalyst with spatially confined metal particles, attaining porous core–shell structure. The synthesis is simple and tunable to independently control, various core and shell structure components from shell thickness to single or multi cores constitution. In addition to our synthetic effort, we have systematically evaluated the unique features afforded by the core–shell morphology based on various model systems for photocatalytic understanding. We demonstrated that the "whereabout" and clustering of Au nanoparticles matter considerably to photocatalytic performance. Furthermore, we have proven the enhanced and prolonged catalytic activity of spatially confined metal cores over conventional surface loaded metal particles, which originates from the structural stability and optimized heterojunction-induced charge transfer attributes.

Results and discussion

The schematic of Fig. 1a shows the structural tuning of the four different designs of TiO_2 nanospheres synthesized with/without Au nanoparticles, as well as surface loaded or spatially confined Au nanoparticles. The samples were synthesized such as to study the effects of Au nanoparticles "whereabouts" and core constitution on photocatalytic properties. In the context of TiO_2 nanostructure synthesis, hydrofluoric acid (HF) has been reported as a structure directing agent to attain better morphological control.[12] However, in this work, TiF_4 precursor is used in place of HF to avoid the direct handling of hazardous acid because the hydrolysis of TiF_4 during hydrothermal reaction promotes the *in situ* release of HF. The introduction of TiF_4 also preferentially exposes the {001} facet of anatase TiO_2, which based on theoretical calculations, has enhanced the reactivity because of higher concentration of low coordination Ti_{5c} centers.[12,13]

Fig. 1b and inset show the SEM image of TiO_2 nanospheres with a rough spherical morphology of an average diameter ~250 nm. The TEM image (Fig. S1†) shows that the TiO_2 nanospheres are made up of randomly shaped TiO_2 nanocrystals, which have self-assembled into a spherical shape. The sizes of the TiO_2 nanospheres can be controlled *via* the amount of TiF_4 added. In addition, different nanospheres sizes ranging from diameter of 200 nm to 1 μm were obtained with increasing TiF_4 (Fig. S2†). Next, Au on TiO_2 or surface loaded Au nanoparticles was synthesized through a physical blending process. The uniform loading of Au nanoparticles onto TiO_2 nanospheres surface can be seen from Fig. 1c and inset. On the other hand, Au@TiO_2, or spatially confined Au nanoparticles, was prepared through the hydrothermal treatment of TiF_4 and Au nanoparticles mixture to promote the formation of core-shell structures (Fig. 1d and e). A series of experiments have proven that both the amounts of TiF_4 and Au nanoparticles affect the shell thickness and the multiplicity of the cores in

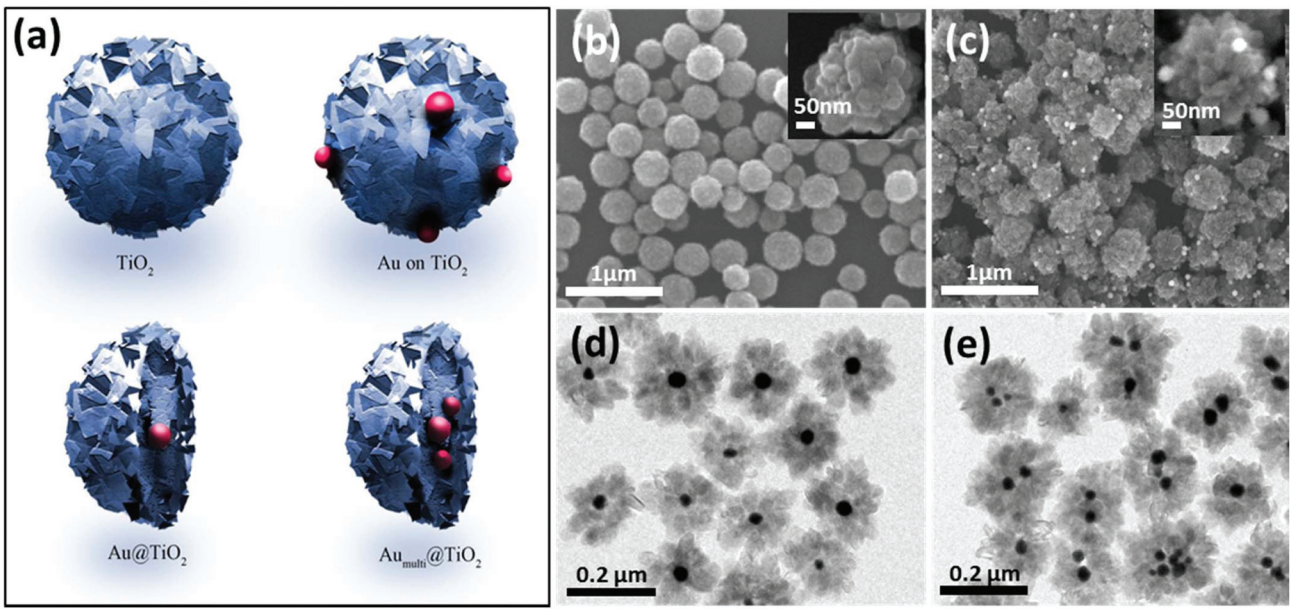

Fig. 1 (a) Schematic of the four different designs of TiO_2 nanospheres synthesized with/without Au nanoparticles, as well as surface loaded or spatially confined Au nanoparticles. SEM images of (b) TiO_2 nanospheres and (c) Au on TiO_2 nanospheres or surface loaded Au nanoparticles on TiO_2 nanospheres. Insets show high magnification of the respective samples. (d–e) TEM images of Au@TiO_2 or spatially confined Au nanoparticles of single and mostly multiple cores.

Au@TiO_2 (the amounts of the reagents are expressed as volume ratios (%) of the stock solutions). At lower TiF_4 volume (<12%), the increase in Au nanoparticles volume ratio effectively decreases the Au@TiO_2 shell thickness (Fig. S2†). The average shell thicknesses (particle sizes) are ~115 nm (250 nm), 90 nm (200 nm), 65 nm (150 nm) and 40 nm (100 nm) with the Au nanoparticles concentrations of 5%, 10%, 20%, and 30% respectively (Fig. S2†). At higher TiF_4 concentrations (>12%), the increase in the Au nanoparticles induced the formation of multiple Au@TiO_2 structures (Fig. S2†). However, when the Au nanoparticles concentrations are too low (<10%), TiO_2 nanospheres without Au cores were observed amongst the single and multiple Au@TiO_2. It is noted that when the TiF_4 and Au nanoparticle concentrations were very high (20% and 40% respectively), some of the nanospheres were observed to have fused, which resulted in Au nanoparticles core clustering (Fig. S2†). The fusing was likely because of the condensation reaction of the surface hydroxyl groups of two adjacent Au@TiO_2 nanospheres. Here, the employed hydrothermal synthesis was demonstrated to be facile and controllable such that the independent tuning of various core and shell structure components from shell thickness to single or multi cores constitution can be demonstrated.

The time-dependent morphological evolution of Au@TiO_2 was studied by taking snapshots at different reaction times. At an initial reaction stage of <15 min, TiF_4 hydrolysates and Au nanoparticles mixture were observed (Fig. S3a–b†). After 30–45 min, TiF_4 hydrolysates were deposited on the Au nanoparticles surface without well-defined structure (Fig. S3c–d†). The supersaturated system results in the formation of the individual TiO_2 nanocrystals observed in the shell structure. Because the surface of Au nanoparticle acts as preferential (heterogeneous) nucleation sites for TiO_2, the core–shell nanostructures are preferentially formed when Au nanoparticles are present. On increasing the reaction time to 1 h, individual core–shell nanospheres were formed (Fig. S3e†). The amount of fluoride ions released at this stage promoted the preferential growth of low-energy (101) TiO_2 facets on Au nanoparticles, which produced nanospheres with relatively sharp and tapered tips. As the TiF_4 hydrolysis continued (Fig. S3f†), the nucleation and growth of TiO_2 species onto the tapered tips evolved into nanospheres with cropped/flattened tips. In addition to the prolong reaction time, the high concentration of F^- ion-terminated (004) crystal planes produced a cropped-tip morphology.[14] The morphology transformation can be attributed to its surface chemistry, in which adsorbate ions impose significant effects on the relative stability of different TiO_2 crystal planes.

A detailed chemical analysis was carried out using EDX mapping to study the elemental composition and distribution throughout the Au@TiO_2 core–shell nanospheres. The images in Fig. 2a–d correspond to the obtained bright field image, O K-edge, Ti K-edge and Au M-edge respectively. It can be seen that the O and Ti signals are found throughout the nanosphere, while the Au signal is located in the center part of the nanosphere. A line scan of a single nanosphere was also performed as plotted in Fig. 2e, which correlates to the elemental mapping of Au and TiO_2 with core–shell structure. The size distribution of Au nanoparticles that was used to confine the

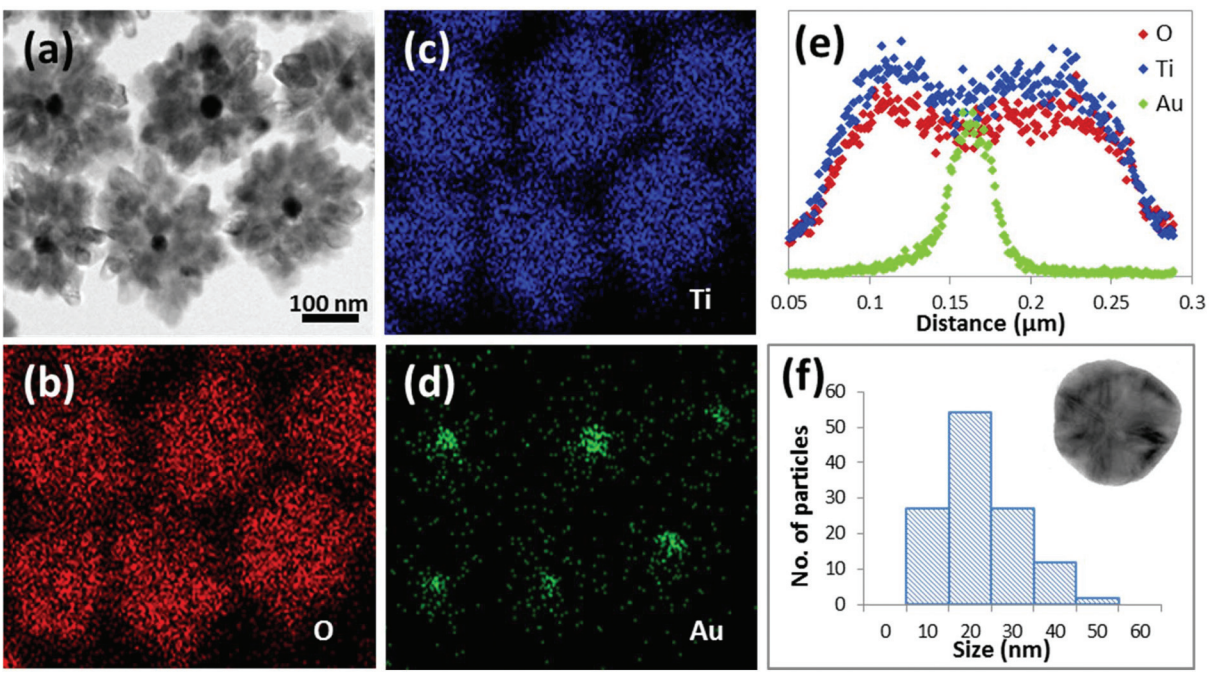

Fig. 2 (a–d) TEM image of the single core Au@TiO_2 and its respective STEM EDX elemental mapping images. (e) Cross-sectional compositional line profiles of a single Au@TiO_2. (f) Histogram of the size distribution of Au nanoparticles. Inset image as-synthesized multi-twinned polyhedron Au nanoparticle.

TiO_2 nanospheres is shown in Fig. 2f. The Gaussian distribution shown in the histogram indicates the size distribution of Au nanoparticles with size 10–50 nm. The Au cores are generally quasi-spherical particles, or more specifically are of multi-twinned polyhedrons (Fig. 2f inset). The quasi spherical shape of the Au cores is found to be well-preserved in the as-synthesized core–shell nanospheres.

The TEM image shown in Fig. 3a indicates the various locations where high resolution imaging is carried out. It is observed from Fig. 3b that a good interface and continuity exist between Au nanoparticle and TiO_2 shell. This suggests a close confinement of the Au nanoparticles within the TiO_2 matrix, thus maximizing the contact area between the interfaces. The light contrast in between the TiO_2 nanoparticles indicates the presence of porosity within the shell. The high-magnification image of the TiO_2 shell (Fig. 3c) shows the adjacent lattice spacing of 0.35 nm, attributed to the (101) lattice planes of the TiO_2 anatase. The high resolution image of Au core (Fig. 3d) shows the lattice fringes of 0.242 and 0.202 nm, which correspond to (111) and (200) of face-centered cubic metallic Au respectively.[16] The XRD spectra (Fig. 3e) of all the nanospheres have shown to possess highly crystalline anatase phase without undergoing any post annealing treatment. The TiO_2 anatase diffraction peaks (101), (004), (200), (105), (211) and (204) are observed at approximately 2θ of 25.3°, 37.8°, 48.1°, 53.9°, 55.1° and 62.8 (JCPDS no. 21-1272), respectively. As compared to the pristine TiO_2 nanospheres, the main anatase diffraction peaks of Au@TiO_2 (single and multiple cores) samples were sharper and stronger, indicating the formation of strong electronic interaction between Au nanoclusters and TiO_2.[15] Furthermore, the Au@TiO_2 spectra for both single and multiple cores exhibit additional diffraction peaks at 38.1°, 44.3° and 64.5°, which can be assigned to the (111), (200) and (220) planes of Au nanoparticles (JCPDS 4-0783). The core–shell nanospheres assume a non-alloy structure as individual Au and TiO_2 diffraction peaks can be obtained. The N_2 adsorption–desorption isotherm and the pore size distribution curves (Fig. 3f) indicate that the Au@TiO_2 is present as mesoporous structures with narrow pore size distributions centered mainly at 12 nm. On the basis of the calculations based on desorption branches using the Brunauer–Emmett–Teller and Barrett–Joyner–Halenda model, the surface area of the Au@TiO_2 is determined to be 38.5 $m^2\ g^{-1}$. The BET analysis shows that the Au@TiO_2 core–shell nanospheres consist of porous shell that strongly favors accessibility to active interfacial sites on Au core. Here, it is concluded that the as-synthesized confined Au cores with porous TiO_2 shells offer passage for water, as well as the satisfactory isolation of nanoparticles against agglomeration.

We have systematically tailored various core and shell components from shell thickness, to core multiplicity in order to evaluate their effects on photocatalytic H_2 production. Fig. 4a shows the photocatalytic H_2 production of different shell thickness with fixed 20 nm Au core. Here, an average H_2 evolution of 188 μmol $h^{-1}\ g^{-1}$ is observed with the shell thicknesses of 65–140 nm (particle sizes between 150–300 nm). However, further increase in shell thickness to 190 and 390 nm (particle size of 400 and 800 nm) decreases the average H_2 evolution drastically to 162 and 51 μmol $h^{-1}\ g^{-1}$ respectively. The decrease in photocatalytic reactivity is likely because of a decrease in the composition ratio of Au to TiO_2 as the shell thickness increases. Next, the synthesis of the core–shell structures was fixed at a shell thickness of ~90 nm equivalent to particle size of diameter 200 nm. The absorption spectra

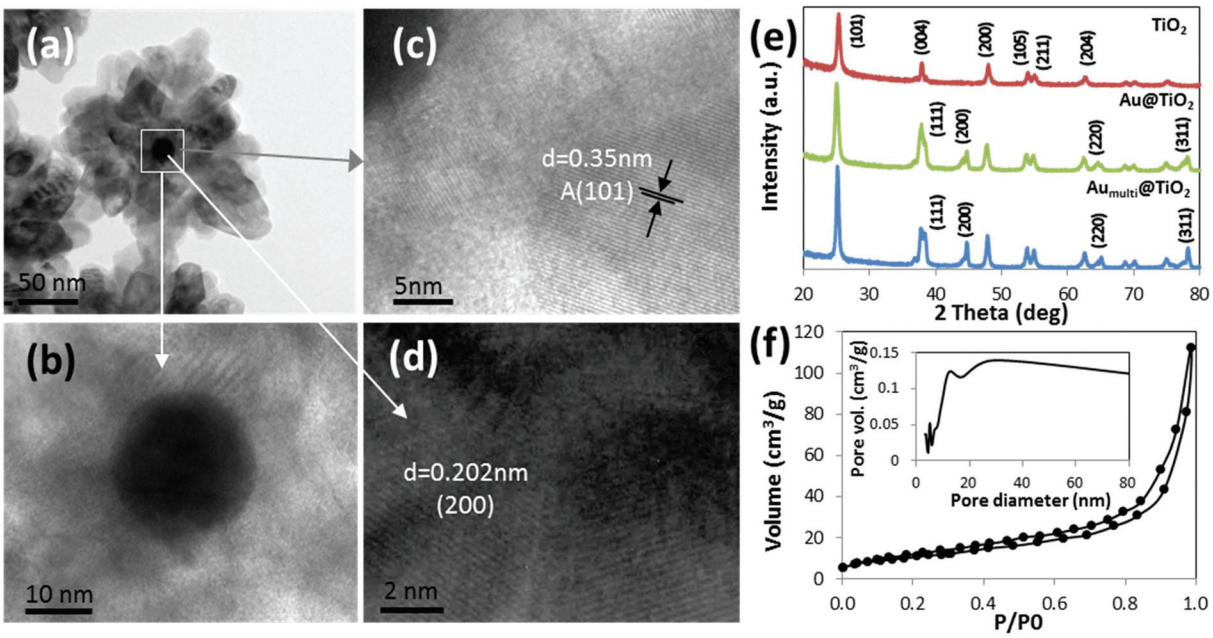

Fig. 3 TEM images of (a) low and (b–d) high magnifications of various locations of Au@TiO_2. (e) XRD spectra of TiO_2 and Au@TiO_2 spectra for both single and multiple cores. (f) N_2 adsorption–desorption isotherm and the pore size distribution curves of single core Au@TiO_2 (inset).

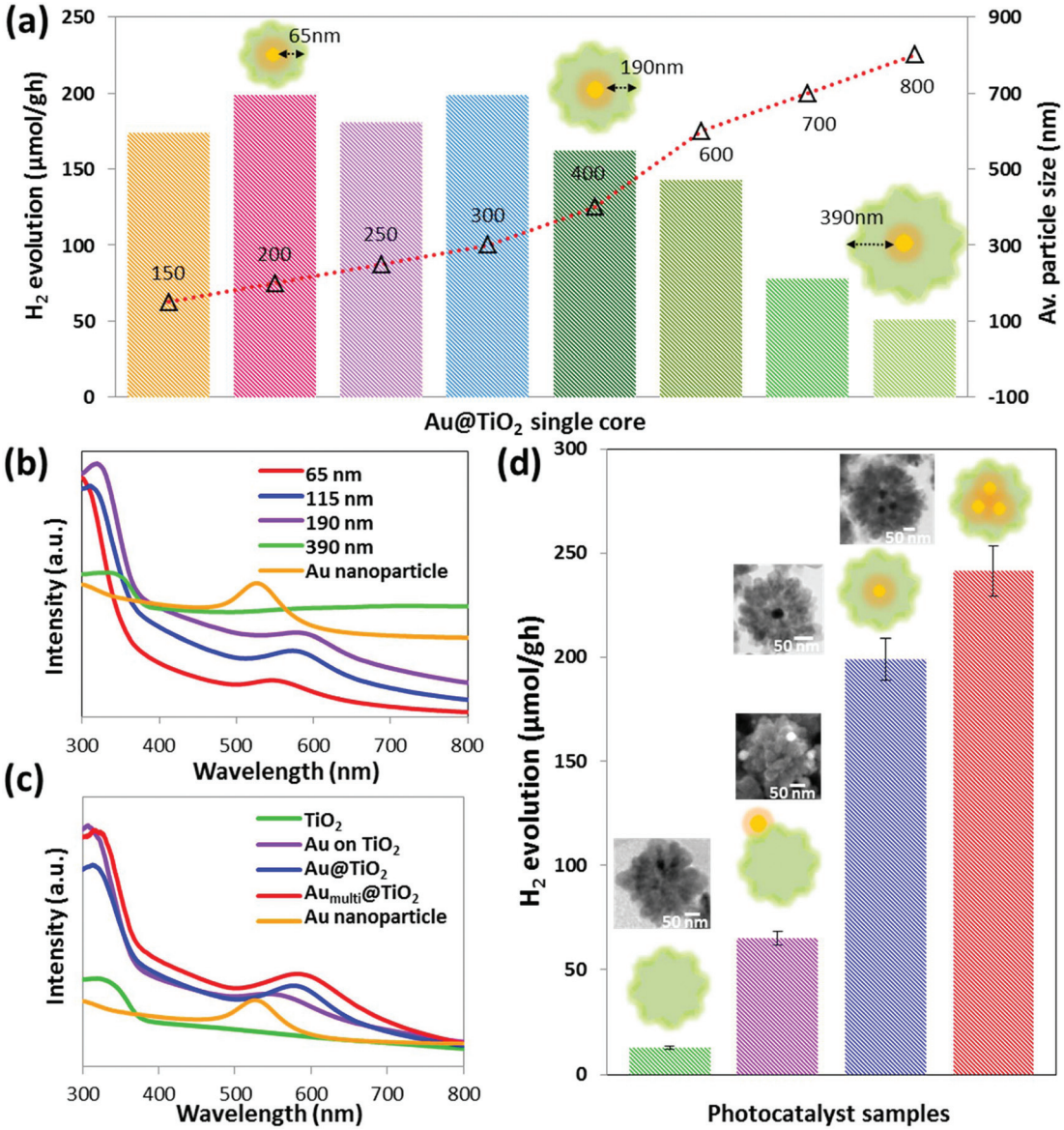

Fig. 4 (a) Photocatalytic H_2 evolution and (b) absorption spectra of different shell thickness with fixed 20 nm Au core. (c) Absorption spectra and (d) H_2 evolution of TiO_2, Au on TiO_2, single and multiple core Au@TiO_2 nanospheres.

(Fig. 4b) show two peaks whereby the weaker visible light absorption peaks are ascribed to the localized surface plasmon resonance (LSPR) response of Au nanoparticles. The physical origin of LSPR is the coherent oscillation of the conduction band electrons induced by the interacting electromagnetic field. A significant LSPR peak red-shift of Au@TiO_2 nanospheres against pure Au nanoparticles (absorption wavelength of ~525 nm) is observed. This clearly reflects that the Au nanoparticles are surrounded by a porous shell of interconnected nanoparticles with a high refractive index. The existence of the oxide shell can be viewed to change the effective refractive index of the medium. Furthermore, the shell thickness is shown to affect the magnitude of the shift where peak shift of ~23, 54 and 65 nm is observed with shell thickness of 65, 115 and 190 nm, respectively. The magnitude of LSPR peaks red shift increase with shell thickness because the effective refractive index of the medium approaches the refractive index of the shell material. However, when the TiO_2 shell thickness increases to 390 nm, the light scattering becomes significant such that the weakening and complete masking of the LSPR peak is evident.[17]

Next, the effect of core content on light absorption and photocatalytic H_2 generation is studied. The pure TiO_2, single and multiple core samples were measured using UV-Vis spectroscopy at room temperature (Fig. 4c). The pure TiO_2 sample shows an absorption peak solely in UV region because of its wide band gap. In contrast, the single and multiple core nanospheres display both UV and visible light absorption because of the presence of Au nanoparticles. In comparison, the multiple core samples exhibit a more intense and broader light

absorption than the single core, both in UV and visible range. The increase in the intensity and broadness of the multiple core plasmon peak with respect to single core nanospheres may be associated to an increase in the Au core content and also an increase in the inter-particle electromagnetic coupling because of the confinement of the individual Au particles in close proximity.[18] The UV-Vis absorption findings complement the photocatalytic performance because the rates of H_2 production increase with the pure TiO_2, single and multiple core nanospheres, corresponding to 13, 199 and 241 μmol h^{-1} g^{-1}, respectively (Fig. 4d). The pure TiO_2 nanospheres without Au core show approximately 15 times less H_2 evolution than the TiO_2 with spatially confined Au cores. This demonstrates the profound effect of the Au core on the photocatalytic activity. Here, the enhancement of the photocatalytic reactivity essentially arises from the unique electronic and optical interactions between the metallic cores and semiconducting shells over a length scale of a few tens of nanometer. Furthermore, it is observed that the modification of the core multiplicity by increasing the Au nanoparticles cores improves the photocatalytic properties. In essence, the probability of charge transfer and reduction of H^+ at the interface, as well as the photogenerated charge carriers that participate in photocatalytic reactions is increased. Finally, the effect of 'whereabout' of the Au nanoparticles, whether loaded on the surface or spatially confined within TiO_2 matrix, is investigated. From the UV-Vis spectra (Fig. 4c), the LSPR peak of Au loaded on TiO_2 surface is observed with a smaller shift against the pure Au spectrum. This is because of the fact that the Au nanoparticles are not embedded in the TiO_2 shell. Hence, the refractive index of the surrounding Au medium does not change significantly. In addition, the intensity of the LSPR peak is weaker, which may suggest a weaker interaction between the TiO_2 shell layer and the Au nanoparticles. Despite the greater exposure of the Au nanoparticles to water for the Au on TiO_2 system, H_2 production was still higher for the Au@TiO_2 case. This strongly suggests that the surface contact area with water is not the only factor that determines the H_2 production rate. As discussed later, electron trapping also plays a dominant role in the H_2 generation. In the case of the Au@TiO_2, the direct nucleation of TiO_2 on the Au core results in a better interface between Au nanoparticles and TiO_2 shell, while the geometric configuration allows optimal area for electronic interaction and also prevents the Au nanoparticles from dislodging. As a result, the rate of H_2 production of the surface loaded Au nanoparticles yields 65 μmol h^{-1} g^{-1} H_2, which is 3–4 times less than the spatially confined Au nanoparticles. These findings highlight that while it is important to incorporate Au metal to TiO_2 for higher photocatalytic performance through enhanced light absorption and charge transfer, the "whereabout" of the Au nanoparticles affects the photocatalytic properties.

In order to understand the carrier dynamics in metal nanoparticle and metal oxide system, time-resolved absorption was measured. The charge transfer between TiO_2 and Au nanoparticle was probed by monitoring the transient absorption decay at 680 nm following 350 nm laser pulse excitation of the Au@TiO_2 nanospheres as shown in Fig. 5a. The band gap excitation of TiO_2 using UV-laser pulse results in charge separation followed by charge recombination and charge-trapping processes. The decay of the transmittance in the picosecond time scale represents the fraction of the electrons that are lost in the recombination process.[19] The transmission-time profiles indicate a faster decay in Au@TiO_2 nanospheres compares with pure TiO_2 system. Therefore, it is obvious that the radiative charge recombination in TiO_2 is substantially suppressed by Au@TiO_2 nanospheres. This quenching phenomenon has been attributed to the effective trapping of photogenerated electron by Au nanoparticles. Furthermore, study on the effect of charge transfer on the photocatalytic hydrogen production performance of the four different designs of TiO_2 nanospheres synthesized with/without Au nanoparticles, as well as surface

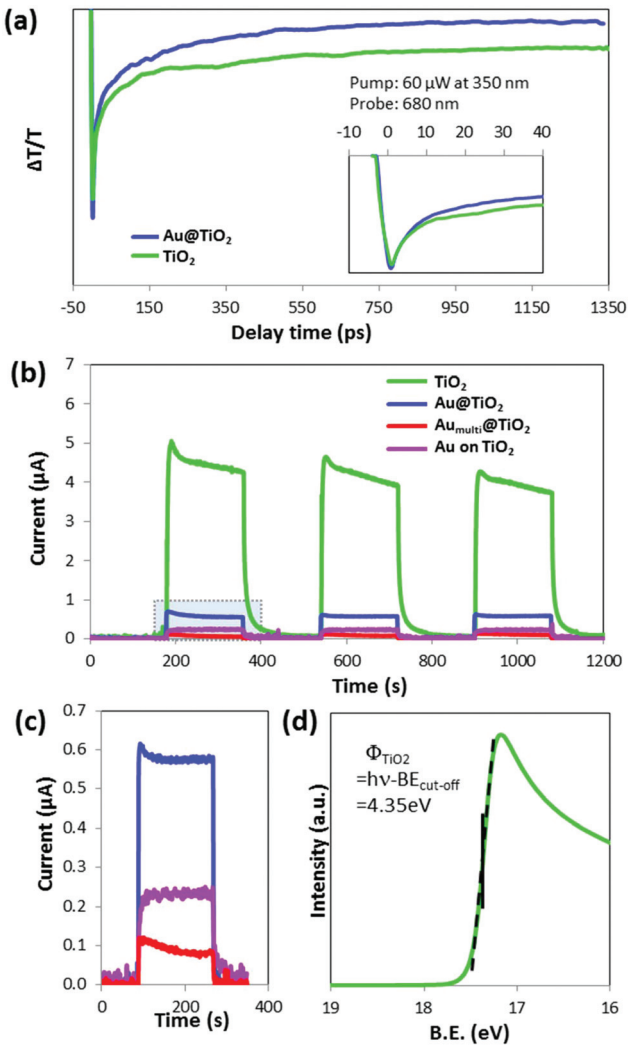

Fig. 5 (a) Transient absorption decay spectra of 350 nm laser pulse excitation of TiO_2 and Au@TiO_2 nanospheres. (b) Photocurrent response of TiO_2 nanospheres, Au on TiO_2 and Au@TiO_2 (single and multiple core) electrodes under UV-Visible irradiation. (c) Magnified plot of (b) at the marked out region. (d) UPS spectra of TiO_2 nanospheres in the valence band region.

loaded or spatially confined Au nanoparticles was carried out using photoelectrochemical (PEC) measurements. Fig. 5b shows the photocurrent of pure TiO_2 nanospheres (~4.25 μA) of almost five times higher than all the TiO_2 with Au nanoparticles systems. The PEC set-up measures the photocurrent by collecting the photogenerated electrons through the photoanode. Upon UV light radiation, a fraction of the photogenerated electrons are transferred to the Au nanoparticles instead of transporting entirely to the transparent electrode and then through the external circuit, thus a lower photocurrent is obtained. Fig. 5c shows the magnified PEC plots of Fig. 5b at the indicated area. The single core Au@TiO_2 system shows a higher photocurrent (~0.57 μA) compares to Au on TiO_2 (~0.34 μA) and multiple core Au_{multi}@TiO_2 (~0.085 μA) system. In regard to the spatially confined Au nanoparticles within TiO_2 shell matrix, the photogenerated electrons are trapped within the Au nanoparticles such that the charge trapping probability increases with the Au nanoparticles content. Hence, the multiple cores Au_{multi}@TiO_2 has lower photogenerated electrons reaching the cathode than the single core Au@TiO_2. In the case of multiple Au nanoparticles that are loaded on TiO_2 nanospheres, a higher photocurrent is measured as compared to multiple cores Au_{multi}@TiO_2 because electrons trapped in Au nanoparticles, which are loaded on the surface of the TiO_2 nanospheres may be transferred to the transparent electrode, thus contribute to the photocurrent. Moreover, the contact area of the multiple Au nanoparticles confined within TiO_2 matrices (Au_{multi}@TiO_2) is higher than that of the Au nanoparticles on TiO_2, hence leading to more charge trapping. From the PEC results, the Au@TiO_2 nanospheres are shown to exhibit superior charge trapping capability, which translates to the inhibition of charge recombination, hence resulted in higher photocatalytic performances.

The band position and band bending of TiO_2 were obtained by UPS (Fig. 5d). In the UPS measurement, binding energy was set as 0 at the Fermi level (Fermi onset: 21.75 eV). The work function of TiO_2 was calculated to be 4.35 eV by using $\varphi_w = h\nu - BE_{cut\text{-}off}$ where $h\nu$ is the corrected kinetic energy (21.75 eV). Based on the information of the band position and band bending obtained, band diagram was drawn to explain this charge trapping effect of the Au nanoparticles (Fig. 6). Au has a higher work function than the TiO_2 semiconductor. In this case, the work function of Au nanoparticles is estimated to be 5.6 eV.[20] When TiO_2 and Au nanoparticles come in contact, the Fermi levels of the Au nanoparticles and TiO_2 align, causing the band bending of TiO_2 and the formation of Schottky barrier. In the presence of UV-Visible irradiation (Fig. 6), the excited electrons in TiO_2 move from the valence band into the conduction band of TiO_2. These electrons in the conduction band of the TiO_2 are available to perform water reduction, which generates hydrogen. However, electrons in the conduction band of TiO_2 can also recombine with the holes in the valence band thus limiting hydrogen production. In the presence of the Au nanoparticles where Fermi level is located at an energy just below the conduction band of TiO_2, the electron in the TiO_2 conduction band can be effectively transferred to the Au nanoparticles.[21] At the semiconductor–water interface, the energy bands of an n-type semiconductor are bent upwards, the corresponding electrical field across the space charge layer drives holes in the valence band of TiO_2 to the surface where the oxidation of sacrificial reagent occurs. Hence, the respective electric fields at both the interfaces enhance the separation of electron–hole pairs, thus reducing the recombination of photogenerated charges. Since the Au@TiO_2 nanospheres are porous, good accessibility of water to Au interface allow hydrogen to be generated.

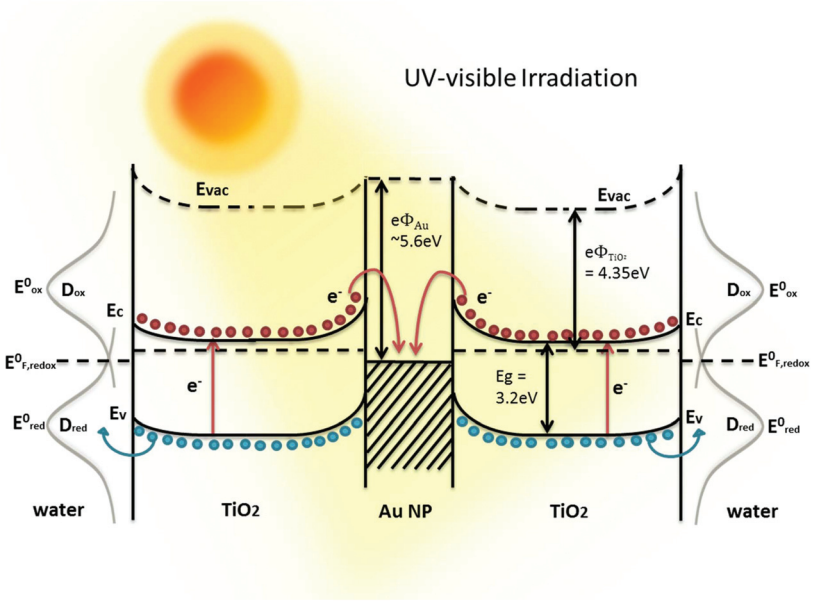

Fig. 6 Proposed photocatalytic mechanism and energy band diagram of the Au@TiO_2 nanospheres under sunlight irradiation.

The photocatalytic stability of three samples of Au on TiO_2 and Au@TiO_2 (single and multiple) core–shell nanospheres were tested through three cycles of two hours sacrificial water splitting experiment. The Au on TiO_2 shows a decrease of 33% in H_2 evolution, whereas the Au@TiO_2 single and multiple core–shell nanospheres exhibit ±5% variation in H_2 evolution (Fig. 7a). Moreover, it is noted that when UV, as well as both UV-visible light are irradiated onto the Au_{multi}@TiO_2 and TiO_2 samples, no increase in the rate of hydrogen production is observed (Fig. S4†). The as-prepared Au@TiO_2 core–shell nanospheres are evidently more stable photocatalyst than Au on TiO_2. In order to investigate the origin of prolonged catalytic activity of the spatially confined metal cores nanospheres as opposed to conventional surface loaded metal particles, The XPS characterization is carried out on the samples after the photocatalytic cycling experiments (Fig. 7b). The Ti2p spectra reveal two peaks, Ti2p 1/2 and Ti2p 3/2 with an energy splitting of 5.7 eV. This confirms the existence of titanium as Ti^{4+}. The Ti2p 3/2 binding energies of Au on TiO_2 and Au@TiO_2 (both single and multiple cores) are at 458.3 and 458.6 eV, respectively. The approximate 0.3 eV shift can be attributed to the transfer of TiO_2 conduction band electron to Au nanoparticles resulting in a decrease in the outer electron cloud density of the Ti ions.[16] This implies a stronger interaction between TiO_2 and Au nanoparticles when they are spatially confined with a core–shell structure.[16,22,23] The Ti2p 3/2 peaks at 458.3–458.6 eV correspond to titanium in the anatase phase, which agrees well with the XRD and TEM structural analyses. The O 1s spectrum of Au on TiO_2 exhibits two peaks at 529.3 and 533.0 eV. The main peak at 529.3 eV is attributed to the oxygen bound to the tetravalent Ti ions, while the shoulder peak is attributed to the adsorbed hydroxyl groups (Ti–OH), defective oxides and/or adsorbed water. It is observed that O1s spectra of Au@TiO_2 (both single and multiple cores) also exhibit a positive shift (approximately 0.6 eV) relative to the Au on TiO_2. Similarly, it has been reported that an increase in binding energies for both Ti2p and O1s can be attributed to strong interaction between Au and TiO_2.[21] Such strong electronic interaction is beneficial to photocatalysis because it is expected to facilitate charge transfer-separation at the inter-

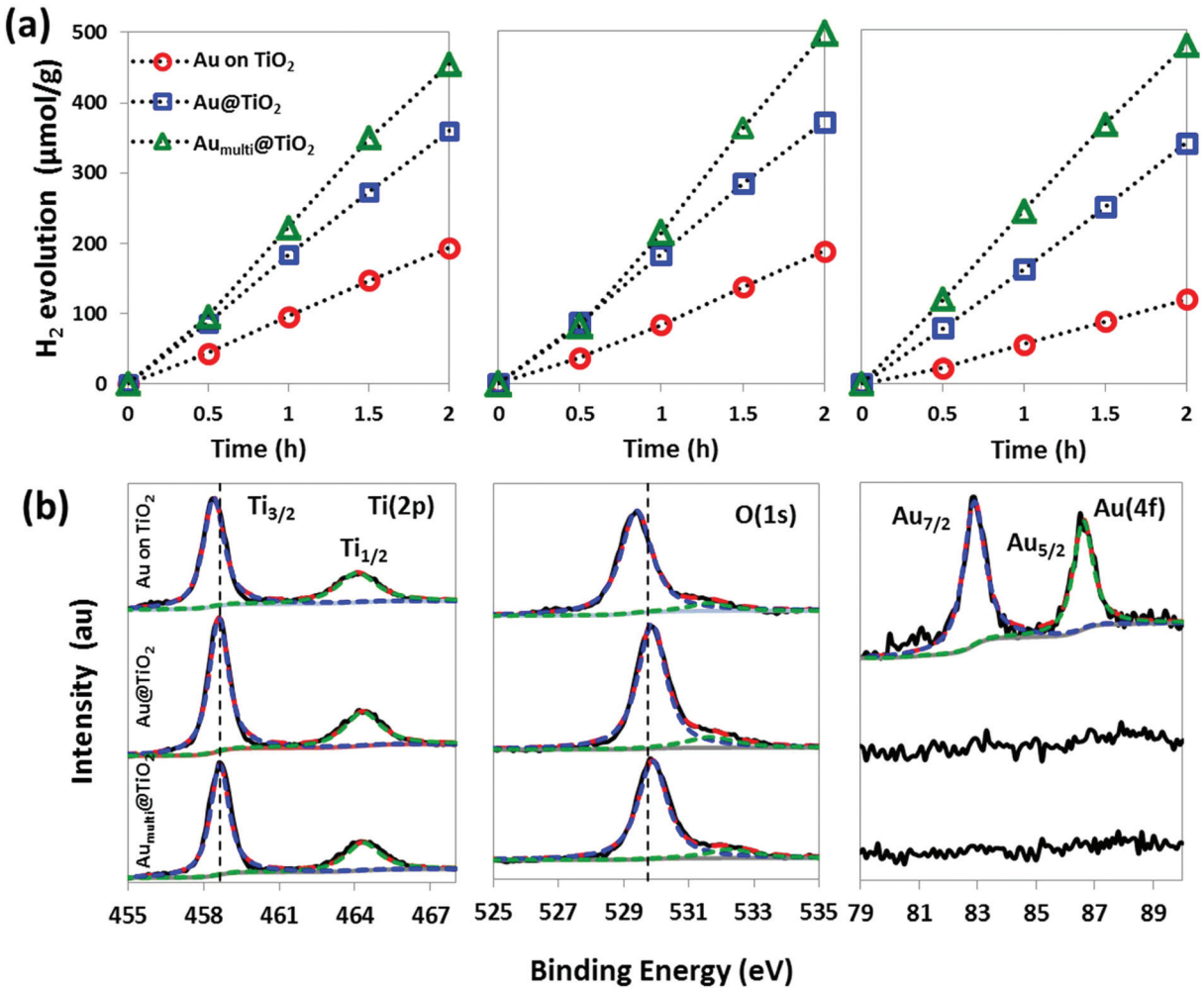

Fig. 7 (a) Photocatalytic H_2 evolution cycles of Au on TiO_2 and Au@TiO_2 (single and multiple) core–shell nanospheres. (b) XPS spectra of the various samples after the photocatalytic cycling experiments.

face. Hence, the sacrificial water splitting of spatially confined Au cores is shown to yield higher H_2 compared to the surface loaded Au nanoparticles. From the Au 4f spectra, it is noted that Au peaks are not detected for both the single and multiple cores Au@TiO_2 samples because the Au nanoparticles are confined within the shell thickness of ~90 nm. This also verifies the homogeneity of Au nanoparticles embedded in TiO_2 matrix. In contrast, Au signal is detected on the Au on TiO_2 sample, where the binding energy of spin–orbit split $Au4f_{7/2}$ is 82.9 eV and Au $4f_{5/2}$ is 86.6 eV, separated by 3.7 eV. This indicates that the Au nanoparticles are present in metallic state on the surface of TiO_2 nanospheres. Hence, it can be inferred that the instability of the catalytic activity of the conventional surface loaded Au nanoparticles is not because of the oxidation of metal particles, but more likely because of the dislodging/leaching of Au nanoparticles, which are loosely attached to the TiO_2 surface. In this regard, it is worth pointing out that the confinement of the Au nanoparticles within TiO_2 matrix not only boosts the charge transfer because of the strong electronic interaction between the core and shell, but also to alleviate Au nanoparticles against leaching. Therefore, another compelling reason to spatially confine the metal nanoparticles with core–shell structure is to ensure prolonged and stable photocatalytic activity.

Conclusions

We demonstrated a facile aqueous method of confining metal nanoparticles within shell matrix *via in situ* encapsulation without the use of template or multiple/post processes. The synthesis route is highly controllable such that the fine structural tuning of core and shell components can offer various model systems for photocatalytic studies. Moreover, we have proven that Au nanoparticles when introduced as cores rather than on the surface, as well as in abundance can dramatically influence the overall photocatalytic performance. We have also demonstrated the effectiveness of multiple Au nanoparticles embedded as core functions as charge accumulator to reduce the recombination of electron–hole pairs. The rational design of novel catalyst has fulfilled various functions, including enhanced light absorption, improved electron–hole separation, accessible redox reactions and stable/prolonged catalytic activity. This work is of fundamental relevance to the design of stable and efficient photocatalysts for sustainable energy and environmental applications.

Experimental section

Synthesis of TiO_2 nanospheres

The different amounts of 0.04 M TiF4 stock solutions ranging from 3 mL to 18 mL were diluted to 100 mL with deionized water and stirred for 10 min. The solutions were transferred to Teflon-lined stainless steel autoclaves and heated in a binder oven at 180 °C for 3 h. After that, the products were cooled to room temperature and separated by centrifuge at 4000 rpm for 5 min, then washed with distilled water. The cycles of separation and washing were repeated three times to remove the remaining ions. The final samples were dried in a 90 °C oven and collected for further use.

Synthesis of Au nanoparticles

4 mL of 0.01 M sodium citrate solution was added to 12 mL of 0.01 M $HAuCl_4$ solution. The mixture was stirred vigorously for 5 min. Then, 3 mL of 0.01 M ascorbic acid was added dropwise to the mixture while stirring. The mixture turned to orchid colour and then rapidly to wine red colour, which indicated gold nanoparticles had been formed.

Synthesis of Au@TiO_2 core–shell

The as-prepared gold nanoparticle solution was stirred continuously for another 10 min. Then, different amounts of 0.04 M TiF_4 stock solutions, ranging from 3 mL to 18 mL were added to the Au nanoparticle solution. The mixture was subsequently diluted to 100 mL with deionized water and transferred to Teflon-lined stainless steel autoclaves. The condition of the hydrothermal reaction and washing process is the same as mentioned above for the synthesis of TiO_2 nanospheres. The yield of Au–TiO_2 heterostructures was calculated to be 82.3% after growth and washing.

Synthesis of Au on TiO_2 structure

The as-prepared Au nanoparticles solution was added into 20 mg of as-prepared TiO_2 nanospheres. The mixture solution was stirred for 12 h. The sample was rinsed with DI water and then centrifuged. The final samples were dried in a 90 °C oven and collected for further use.

Materials characterization

The scanning electron microscopy (SEM) characterization was carried out using a JEOL FEG JSM 6700F field-emission operating at 15 kV. X-ray photoelectron spectroscopy (XPS), VG ESCALAB 220I-XL system equipped with an Mg Kα X-ray source was employed chemical for composition studies. The crystalline structures were analyzed using transmission electron microscopy (TEM, Phillips FEG CM300) operated at 200 kV and X-ray diffraction (XRD, Philips X-ray diffractometer equipped with graphite-monochromated Cu Kα radiation at λ = 1.541 Å). Absorption spectra were obtained using a Shimadzu UV-3600 UV-vis spectrophotometer. Brunauer–Emmett–Teller (BET) measurements were conducted using Quantachrome Nova 1200 with N_2 as the adsorbate at liquid nitrogen temperature. Photoelectrochemical (PEC) samples were prepared on fluorine doped tin oxide (FTO) substrates (QZ hybrid supplies, <10 Ω per sq) using a doctor blade method. Slurries were prepared from the various nanostructure powders and deionised water, which were then applied on the surface of the FTO glass using a glass rod. The coated FTO glass substrates were dried at 70 °C on a hot plate. The PEC measurements were carried out with a potentiostat in a 2 electrode configuration, using the photoanode prepared on FTO

and a Pt counter electrode with 0 V bias in 0.1 M Na_2SO_4 electrolyte. The ultraviolet photoelectron spectroscopy (UPS) was performed with a He I (21.21 eV) radiation (VG Scientific ESCA Lab Mark 2). The binding energy of all spectra was calibrated using a gold (Au) metal, at which the Fermi onset is located at kinetic energy of 21.75 eV. The H_2 evolution measurements were carried out using 30 mg of photocatalyst and 10 mL DI water (10% methanol) contained in a quartz vial and illuminated with a 300 W Xe lamp (Excelitas, PE300BFM). The wavelength range and light intensity of the Xe lamp is 300–1100 nm and 100 mW cm^{-2}, respectively. The reaction mixture was purged with Ar gas for 15 min prior to measurements. The reaction mixture was syringe drawn (100 μl) to sample the gas composition using gas chromatographer (Shimadzu, GC-2014AT).

Acknowledgements

This work is supported by the A*Star grant R-263-000-A96-305.

References

1 D. Djoumessi Lekeufack, A. Brioude, A. Mouti, J. G. Alauzun, P. Stadelmann, A. W. Coleman and P. Miele, Core-shell Au@(TiO_2,SiO_2) nanoparticles with tunable morphology, *Chem. Commun.*, 2010, **46**, 4544–4546.
2 G. Oldfield, T. Ung and P. Mulvaney, Au@SnO_2 Core-Shell Nanocapacitors, *Adv. Mater.*, 2000, **12**, 1519–1522.
3 T. Hirakawa and P. V. Kamat, Charge Separation and Catalytic Activity of Ag@TiO_2 Core-Shell Composite Clusters under UV-Irradiation, *J. Am. Chem. Soc.*, 2005, **127**, 3928–3934.
4 C. Z. Wu, Z. Y. Lim, C. Zhou, W. G. Wang, S. Zhou, H. Yin and Y. Zhu, A soft-templated method to synthesize sintering resistant Au-mesoporous-silica core-shell nanocatalysts with sub-5 nm single-cores, *Chem. Commun.*, 2013, **49**, 3215–3217.
5 J. H. Byeon and Y. W. Kim, Au-TiO_2 Nanoscale Heterodimers Synthesis from an Ambient Spark Discharge for Efficient Photocatalytic and Photothermal Activity, *ACS Appl. Mater. Interfaces*, 2014, **6**, 763–767.
6 J. Lu, B. Fu, M. C. Kung, G. Xiao, J. W. Elam, H. H. Kung and P. C. Stair, Coking and sintering resistant palladium catalysts achieved through atomic layer deposition, *Science*, 2012, **335**, 1205–1208.
7 S. Ikeda, S. Ishino, T. Harada, N. Okamoto, T. Sakata, H. Mori, S. Kuwabata, T. Torimoto and M. Matsumura, Ligand-Free Platinum Nanoparticles Encapsulated in a Hollow Porous Carbon Shell as a Highly Active Heterogeneous Hydrogenation Catalyst, *Angew. Chem., Int. Ed.*, 2006, **45**, 7063–7066.
8 I. Lee, Q. Zhang, J. Ge, Y. Yin and F. Zaera, Encapsulation of Supported Pt Nanoparticles with Mesoporous Silica for Increased Catalyst Stability, *Nano Res.*, 2011, **4**, 115–123.
9 J. Ge, Q. Zhang, T. Zhang and Y. Yin, Core-Satellite Nanocomposite Catalysts Protected by a Porous Silica Shell: Controllable Reactivity, High Stability, and Magnetic Recyclability, *Angew. Chem., Int. Ed.*, 2008, **47**, 8924–8928.
10 X. Z. Kong, W. Jiang, X. Jiang and X. Zhu, Preparation of core-shell and hollow polyurea microspheres via precipitation polymerization using polyamine as crosslinker monomer, *Polym. Chem.*, 2013, **4**, 5776–5784.
11 H. Dong, M. Zhu, J. A. Yoon, H. Gao, R. Jin and K. Matyjaszewski, One-Pot Synthesis of Robust Core/Shell Gold Nanoparticles, *J. Am. Chem. Soc.*, 2008, **130**, 12852–12853.
12 H. G. Yang, C. H. Sun, S. Z. Qiao, J. Zou, G. Liu, S. C. Smith, H. M. Cheng and G. Q. Lu, Anatase TiO_2 single crystals with a large percentage of reactive facets, *Nature*, 2008, **453**, 638–641.
13 R. Menzel, A. Duerrbeck, E. Liberti, H. C. Yau, D. McComb and M. S. P. Shaffer, Determining the Morphology and Photocatalytic Activity of Two-Dimensional Anatase Nanoplatelets Using Reagent Stoichiometry, *Chem. Mater.*, 2013, **25**, 2137–2145.
14 X. F. Wu, H. Y. Song, J. M. Yoon, Y. T. Yu and Y. F. Chen, Synthesis of Core-Shell Au@TiO_2 Nanoparticles with Truncated Wedge-Shaped Morphology and Their Photocatalytic Properties, *Langmuir*, 2009, **25**, 6438–6447.
15 Y. Konishi, I. Tanabe and T. Tatsuma, Stable spectral dip formation and multicolour changes of plasmonic gold nanoparticles on TiO_2, *Chem. Commun.*, 2013, **49**, 606–608.
16 Y. Liu, L. F. Chen, J. C. Hu, J. L. Li and R. Richards, TiO_2 Nanoflakes Modified with Gold Nanoparticles as Photocatalysts with High Activity and Durability under near UV Irradiation, *J. Phys. Chem. C*, 2010, **114**, 1641–1645.
17 P. Ramasamy, D. M. Seo, S. H. Kim and J. W. Kim, Effects of TiO_2 shells on optical and thermal properties of silver nanowires, *J. Mater. Chem.*, 2012, **22**, 11651–11657.
18 S. K. Ghosh and T. Pal, Interparticle Coupling Effect on the Surface Plasmon Resonance of Gold Nanoparticles: From Theory to Applications, *Chem. Rev.*, 2007, **107**, 4797–4862.
19 V. Subramanian, E. E. Wolf and P. V. Kamat, Catalysis with TiO_2/Gold Nanocomposites. Effect of Metal Particle Size on the Fermi Level Equilibration, *J. Am. Chem. Soc.*, 2004, **126**, 4943–4950.
20 N. T. Khoa, S. W. Kim, D. H. Yoo, E. J. Kim and S. H. Hahn, Size-dependent work function and catalytic performance of gold nanoparticles decorated graphene oxide sheets, *Appl. Catal., A*, 2014, **469**, 159–164.
21 Z. Bian, T. Tachikawa, W. Kim, W. Choi and T. Majima, Superior electron transport and photocatalytic abilities of metal nanoparticle-loaded TiO_2 superstructures, *J. Phys. Chem. C*, 2012, **116**, 25444–25453.
22 D. Zhang, G. Li, F. Wang and J. C. Yu, Green synthesis of a self-assembled rutile mesocrystalline photocatalyst, *CrystEngComm*, 2010, **12**, 1759–1763.
23 Y. Do, J. S. Choi, S. K. Kim and Y. Sohn, The interfacial nature of TiO_2 and ZnO nanoparticles Modified by gold nanoparticles, *Bull. Korean Chem. Soc.*, 2010, **31**, 2170–2174.

